IOE | Intelligent Opto-Electronics

Decomposition and mode-weight estimation of mixed-mode OAM beams via diffractive neural networks

Lijun Wang, Jingdong Wang, Yingli Ha, Yinghui Guo, Mingfeng Xu, Mingbo Pu, Yunjie Liu and Xiangang Luo

Citation: Wang LJ, Wang JD, Ha YL, et al. Decomposition and mode-weight estimation of mixed-mode OAM beams via diffractive neural networks. *Intelligent Opto-Electronics* **2**, 250011 (2026).

Received: 23 October 2025; Accepted: 17 December 2025; Published online: 25 March 2026

Related articles

Pluggable multitask diffractive neural networks based on cascaded metasurfaces
Cong He, Dan Zhao, Fei Fan, Hongqiang Zhou, Xin Li, Yao Li, Junjie Li, Fei Dong, Yin-Xiao Miao, Yongtian Wang, Lingling Huang
Opto-Electronic Advances 2024, **7**(2): 230005 doi: 10.29026/oea.2024.230005

Multi-dimensional multiplexing optical secret sharing framework with cascaded liquid crystal holograms
Keyao Li, Yiming Wang, Dapu Pi, Baoli Li, Haitao Luan, Xinyuan Fang, Peng Chen, Yanqing Lu, Min Gu
Opto-Electronic Advances 2024, **7**(1): 230121 doi: 10.29026/oea.2024.230121

Tailoring electron vortex beams with customizable intensity patterns by electron diffraction holography
Pengcheng Huo, Ruixuan Yu, Mingze Liu, Hui Zhang, Yan-qing Lu, Ting Xu
Opto-Electronic Advances 2024, **7**(2): 230184 doi: 10.29026/oea.2024.230184

Integrated photonic synapses, neurons, memristors, and neural networks for photonic neuromorphic computing
Shufei Han, Weihong Shen, Min Gu, Qiming Zhang
Opto-Electronic Technology 2025, **1**(3): 250011 doi: 10.29026/oet.2025.250011

More related articles in Opto-Electronic Journals Group website

IOE | Intelligent Opto-Electronics

Article

March 2026, Vol. 2, No. 1

Open Access

Decomposition and mode-weight estimation of mixed-mode OAM beams via diffractive neural networks

Lijun Wang[1,2,3†], Jingdong Wang[1,2,3†], Yingli Ha[1,2,3], Yinghui Guo[1,2,3,4], Mingfeng Xu[1,2,3,4], Mingbo Pu[1,2,3], Yunjie Liu[4,5] and Xiangang Luo[1,2,3]*

Abstract: Beams carrying orbital angular momentum (OAM) have attracted considerable interest in high-capacity optical communication owing to their infinite-dimensional state space. Conventional methods for detecting OAM modes face significant limitations, including bulky systems, slow response times, and restricted detection ranges. Although deep learning algorithm have shown promise in mitigating some of these challenges, the characterization of mode distributions within mixed-mode OAM beams has received limited attention. We propose an all-optical, end-to-end approach for decomposing mixed-mode OAM beams and estimating their mode weights using diffractive deep neural network (D^2NN). The network directly maps the incident optical field to outputs that both identify the constituent OAM modes and estimate their relative contributions. Numerical simulations demonstrate that the method can accurately recover the weights of up to 21 hybrid modes. Moreover, it maintains strong robustness under atmospheric perturbations, with the relative error remaining below 7%. This approach enables precise and efficient reconstruction of the OAM beams across varying numbers of modes, offering broad potential in multidimensional information encoding, quantum information processing, and optical computing.

Keywords: diffractive optical neural networks; orbital angular momentum; mixed-mode decomposition; mode-weight estimation

DOI:

Citation: Wang LJ, Wang JD, Ha YL et al. Decomposition and mode-weight estimation of mixed-mode OAM beams via diffractive neural networks. *Intell Opto-Electron* **2**, 250011 (2026).

1 Introduction

Optical beams carrying orbital angular momentum (OAM), characterized by their helical phase fronts, have attracted extensive attention due to their fundamental significance and applications in optical manipulation[1–3], microscopy[4–6], and rotational sensing[7–9]. Numerous mature techniques have been developed for generating OAM beams[10–12], which has greatly expanded their use in various optical applications. As these applications increasingly depend on precise modal content, reliable identification of OAM modes has become a critical requirement. A variety of reliable approaches have been demonstrated for identifying single-mode OAM states, such as reference wavefront interference[13–15], aperture- or grating-based diffraction techniques[16–19], and metasurface-based mode-sorting methods[20,21]. By contrast, accurately characterizing superimposed multimode vortices remains a considerable challenge. Such hybrid beams offer great promise for expanding encoding dimensions[22,23], enhancing channel capacity[24], and supporting advanced modulation formats[25]. However, existing detection schemes for multi-mode OAM beams typically rely on complex cascaded optical systems[26] or hybrid optical–electronic approaches[27], which limits their efficiency in retrieving multiple modal components within a single measurement and constrains their scalability when the number of detectable modes increases or the mode space becomes larger.

Received: 23 October 2025

Accepted: 17 December 2025

[1]State Key Laboratory of Optical Field Manipulation Science and Technology, Institute of Optics and Electronics, Chinese Academy of Sciences, Chengdu 610209, China; [2]Research Center on Vector Optical Fields, Institute of Optics and Electronics, Chinese Academy of Sciences, Chengdu 610209, China; [3]College of Materials Science and Opto-Electronic Technology, University of Chinese Academy of Sciences, Beijing 100049, China; [4]Sichuan Provincial Engineering Research Center of Digital Materials; [5]Tianfu Xinglong Lake Laboratory, Chengdu 610299, China.

[†]These authors contributed equally to this work.

*Correspondence: XG Luo, E-mail: lxg@ioe.ac.cn

With the rapid advancement of artificial intelligence algorithms, neural network–based strategies have opened new avenues for the precise analysis and efficient processing of complex optical fields[28–31]. Wang, J et al. introduced a hybrid approach that combines optical diffraction with convolutional neural network post-processing to identify the OAM beams of multi-mode mixtures[32]. However, the system architecture and data processing are relatively complex, and scaling to a larger mode set necessitates further increases in both system and data complexity. Another strategy relies on employing coaxial interference between OAM beams and Gaussian beams followed by Fourier-domain analysis for spectral extraction[33], yet this technique demands stringent experimental stability. Hybrid optical–electronic frameworks have also been investigated, where an optical neural network first analyzes positive and negative topological charges, followed by a fully connected electronic neural network for spectral prediction[34]. This cascading design allows accurate mode identification but introduces substantial implementation complexity and demands precise coordination between optical and electronic components. Overall, current methods still suffer from deficiencies in detection efficiency, system simplicity, and scalability.

Since Lin, X first proposed the diffractive deep neural network (D^2NN) in 2018[35], this method has become an important direction in optical neural network research because it enables all-optical neural network inference[36]. D^2NN has been widely applied in scenarios such as beam shaping[37,38], image reconstruction[39–41], and optical encryption[42–44], and have gradually been introduced into OAM detection. Compared with traditional techniques, D^2NN-based approaches offer higher efficiency. Early studies have used D^2NN for OAM mode classification, analyzing how factors such as the number of diffractive layers and turbulence strength affect recognition accuracy[45]. Subsequent developments have further enhanced the approach, enabling classifiers that can identify multiple degrees of freedom of optical beams within a single framework[46]. However, existing studies have mostly focused on classification within a limited mode range with fewer efforts addressing the reconstruction of full spectral distributions in mixed-mode beams.

In this study, we propose a hybrid OAM modes recognition system based on optical diffraction neural networks. This approach performs end-to-end optical inference, in which the incident OAM optical field is directly mapped to the light-intensity distribution at the output plane through a sequence of diffractive layers, without complex post-processing. We conducted tests on single-mode and arbitrarily proportioned mixed-mode OAM beams within the range of 21 modes (topological charge l = -10 to 10, radial index p = 0). The simulation results demonstrate that the proposed method maintains high recognition accuracy for both single-mode and multi-mode mixed beams, and exhibits strong robustness against non-uniform mode proportion mixing and low-intensity modes. Even under the perturbation of atmospheric turbulence, our model still maintains to show good recognition ability. In practice, the four phase plates in the D^2NN can be implemented either as metasurfaces for compact chip-scale devices or as programmable spatial light modulators (SLMs) for flexible prototyping. Our findings are expected to contribute to the development of OAM-enabled optical communication and show potential for applications in high-speed, large-capacity information processing systems.

2 Methods

As shown in Fig.1, the OAM detection device consists of four diffractive phase screens and an output layer. When the OAM beam illuminates the phase screen, a specific light intensity distribution is formed at the location of the output layer by optical diffraction. Since the light intensity of each region is different, topological charges and weights of different beams can be identified by calculating the electric field distribution of each region. The OAM detection device enables precise characterization of both single-mode and spatially multiplexed OAM beams.

The expression for the OAM beam in cylindrical coordinates is

$$U(r,\phi,z) = U_0(r,z)\mathrm{e}^{-\mathrm{j}kz}\mathrm{e}^{\mathrm{j}l\phi}\ , \tag{1}$$

where l represents the topological charge and ϕ is the azimuthal angle in cylindrical coordinates. $U_0\ (r,\ z)$ represents the amplitude term, and j denotes the imaginary unit. To model the OAM beam more specifically, we use a common Laguerre-Gaussian (LG) beam[47,48], and its complex amplitude expression in cylindrical coordinates is

$$\begin{aligned} LG_{lp}\left(r,\phi,z\right) = &\frac{C_{lp}}{w\left(z\right)}\left(\frac{\sqrt{2}r}{w\left(z\right)}\right)^{|l|}L_p^{|l|}\left(\frac{2r^2}{w^2\left(z\right)}\right)\mathrm{e}^{\frac{-r^2}{w^2(z)}}\mathrm{e}^{\frac{-\mathrm{j}kr^2}{2R(z)}} \\ &\times \mathrm{e}^{-\mathrm{j}(2p+|l|+1)\zeta(z)}\mathrm{e}^{-\mathrm{j}kz}\mathrm{e}^{\mathrm{j}l\phi}\ , \end{aligned} \tag{2}$$

where p represents the radial index that determines the number of radial nodes in the beam, and l represents the topological charge that defines the helical phase structure and the associated orbital angular momentum. C_{lp} is a normalization constant. $L_p^{|l|}\left(x\right)$ is the generalized laguerre polynomial and k is the wave number. $z_R = \pi w_0^2/\lambda$ denotes Rayleigh length, where λ is the working wavelength and w_0 is the waist radius. $w\left(z\right) = w_0[1+\left(z/z_R\right)^2]^{1/2}$ indicates the radius of the light spot. $R\left(z\right) = z\left[1+\left(z_R/z\right)^2\right]$ represents radius of curvature of the wavefront. $\zeta\left(z\right) = \arctan\left(z/z_R\right)$ refers to Gouy phase.

We generated a total of 10000 datasets, each consisting of an incident optical field and its corresponding label. Among them, 8400 samples were used for training, including 2100

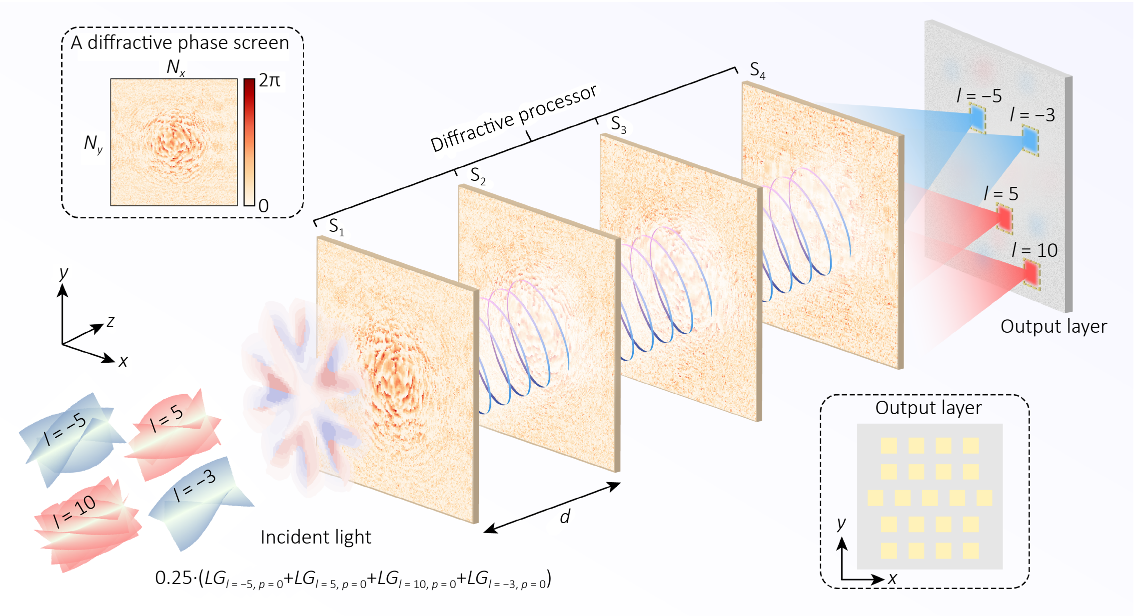

Fig. 1 | Schematic of LG mode recognition device based on diffractive optical neural network. The incident light can be a single-mode LG beam or a mixed-mode LG beam. The diffractive processor contains four layers of phase screens (inset, upper left), with N_x = N_y = 200. At the output layer (inset, lower right), 21 rectangular detection regions are assigned to different LG modes, enabling recognition by measuring the light intensity in each region.

single-mode beam samples and 6300 mixed-mode beam samples. The mixed-mode samples were generated by randomly selecting multiple LG modes to form superpositions, including both equal-weighted and unequal-weighted mixtures (3150 samples each). The number of constituent modes in a mixed-mode sample varies from 2 up to all 21 modes included in the dataset, with each mode carrying its own intensity weight in the superposition. The remaining 1000 and 600 datasets were allocated to validation and testing, respectively, with comparable proportions of single- and mixed-mode beams. The incident optical field is represented by a 200 × 200 matrix of complex amplitudes, and the label is a 21 × 1 vector whose elements represent the weights of the corresponding OAM modes, ordered sequentially according to topological charges from −10 to 10. As illustrated in Fig. 1, the four OAM beams ($\mathrm{LG}_{l=-5,\,p=0}$, $\mathrm{LG}_{l=-3,\,p=0}$, $\mathrm{LG}_{l=5,\,p=0}$, and $\mathrm{LG}_{l=10,\,p=0}$) are mixed with the same weight of 0.25, resulting in the label is [0, 0, 0, 0, 0, 0.25, 0, 0.25, 0, 0, 0, 0, 0, 0, 0, 0.25, 0, 0, 0, 0, 0.25].

The optical field propagation process of diffraction phase screens can be described according to the Rayleigh-Sommerfeld diffraction theory[49]:

$$U(x,y,z) = \frac{z}{\mathrm{j}\lambda}\iint_{-\infty}^{\infty} U(x',y',0)\,\frac{\mathrm{e}^{\mathrm{j}kr}}{r^2}\mathrm{d}x'\mathrm{d}y' \ , \tag{3}$$

where $U(x', y', 0)$ and $U(x, y, z)$ denote the complex amplitude on the previous diffraction screen and the current diffraction screen, respectively. $r = [(x-x')^2 + (y-y')^2 + z^2]^{1/2}$ is the distance between the two observation points.

Figure 2(a) illustrates the network training process based on the diffraction principle. During network training, each phase unit on the phase screen acts as a neuron. During forward propagation, according to diffraction theory, each neuron can be considered a secondary wave source:

$$w_i^s(x,y,z) = \frac{z - z_i^s}{d^2}\left(\frac{1}{2\pi d} + \frac{1}{j\lambda}\right)\mathrm{e}^{\mathrm{j}\frac{2\pi d}{\lambda}} \ , \tag{4}$$

where s represents the s-th layer of the network, and i represents the i-th neuron located at (x_i, y_i, z_i) of layer s. λ is the working wavelength, and $d = [(x-x_i)^2 + (y-y_i)^2 + (z-z_i)^2]^{1/2}$ represents the distance between two neurons. The complex amplitude of this secondary wave is determined by the product of the incident optical field and the transmission coefficient at that location. The output function of the i-th neuron in the s-th layer is

$$n_i^s(x,y,z) = w_i^s(x,y,z)\cdot t_i^s \cdot \sum_k n_k^{s-1}(x_i,y_i,z_i) \tag{5}$$

can be simplified as

$$n_i^s = w_i^s \cdot t_i^s \cdot m_i^s \ , \tag{6}$$

where $m_i^s = \sum_k n_k^{s-1}(x_i,y_i,z_i)$ is the incident wave to the i-th neuron in the s-th layer, and t_i^s is the complex transmission coefficient, which can be decomposed into an amplitude and a phase

$$t_i^s = a_i^s \cdot \mathrm{e}^{\mathrm{j}\phi_i^s} \ . \tag{7}$$

For a pure-phase type D²NN in this work, the amplitude term $a_i^s = 1$ (neglecting optical losses), and each neuron

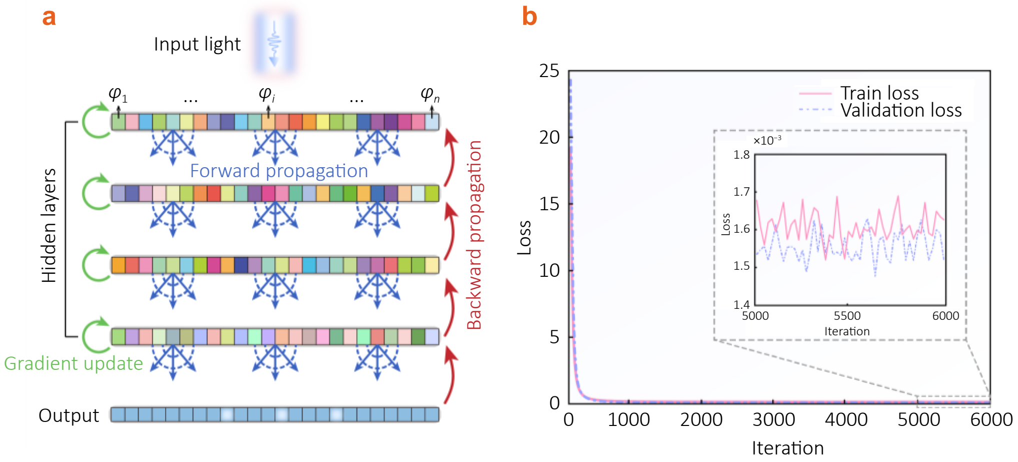

Fig. 2 | Principles of the network and the training loss. (a) Schematic diagram of the network principle. (b) Evolution of the network loss value with the iterations.

performs only phase modulation.

As shown in Fig. 2(a), the incident optical field sequentially passes through multiple phase screens, where each phase screen is contains 200 × 200 phase cells with a size of 1 μm × 1 μm. Each layer modulates the optical field by introducing a spatially dependent phase delay, followed by diffractive propagation in free space, which achieves a step-by-step feature mapping of the incident beam. The entire process can be considered an end-to-end neural network, with the phase values of each pixel on the phase plates acting as trainable parameters. The propagation distance d between adjacent phase screens is fixed at 200 μm in this work. On the output plane, the 200 μm × 200 μm area is divided into 21 rectangular detection regions, in which each region measures 15 μm × 15 μm, corresponding to 21 OAM modes (from $l = -10$ to $l = 10$, $p = 0$). Considering that the weights of the 21 modes are non-negative and sum to unity, the collected light intensities from the 21 detection regions are transformed into a mode-weight vector through a softmax operation. This operation ensures that all predicted mode weights lie within [0,1] and collectively sum to one. The loss function is defined as the mean squared error (MSE) between the predicted intensity vector and the target intensity vector, computed over the 21 detection regions:

$$Loss = \frac{1}{21}\sum_{k=1}^{21}\left(\hat{I}_k - I_k\right)^2 , \qquad (8)$$

where I_k and $\hat{I}_k$denote the target and predicted intensities within the k-th region, respectively. This loss is minimized using backpropagation and gradient descent to update the phase parameters of the diffractive layers. The training loss and validation loss finally reach 0.00151 and 0.00162 after 6000 iterations as shown in Fig. 2(b).

3 Results and discussion

3.1 Single-mode classification

To evaluate the discrimination ability of the trained diffraction processor under single-mode conditions, we performed blind tests on LG beams with random initial phases. As shown in Fig. 3(a-c), for incident beams with modes: $l = -1$, $l = 10$, and $l = 4$, the network predicts energy peaks on the corresponding output channels that are consistent with the true values with good sidelobe suppression. Here, we define the relative error of the prediction results as

$$Error_{\text{rel}} = \frac{\left|w_{\text{prediction}} - w_{\text{truth}}\right|}{w_{\text{truth}}} , \qquad (9)$$

where $w_{\text{prediction}}$ and w_{true} represent the predicted and ground-truth mode weights, respectively. All the relative errors are less than 7%, indicating that the model is able to perform mode recognition consistently and accurately under unimodal output conditions. In order to show more comprehensively the prediction results of the model for all modes, we sampled 100 datasets per mode for blind testing. As shown in Fig. 3(d), the main diagonal of the confusion matrix is significantly prominent, while the off-diagonal entries are sparse and of low magnitude. The overall accuracy is over 98.5%. Minor errors are concentrated between neighboring orders, which is primarily due to the fact that physically similar topological charges are susceptible to energy leakage and channel crosstalk under finite aperture and sampling conditions.

A point to emphasize is that when p is fixed, the l and $-l$ LG beams have the same intensity distribution but show opposite spiral phases. Therefore, conventional detection schemes that rely only on intensity cannot distinguish between positive and negative chirality. Our approach utilizes multilayer diffractive elements to shape the incident complex amplitude wavefront, mapping beams carrying

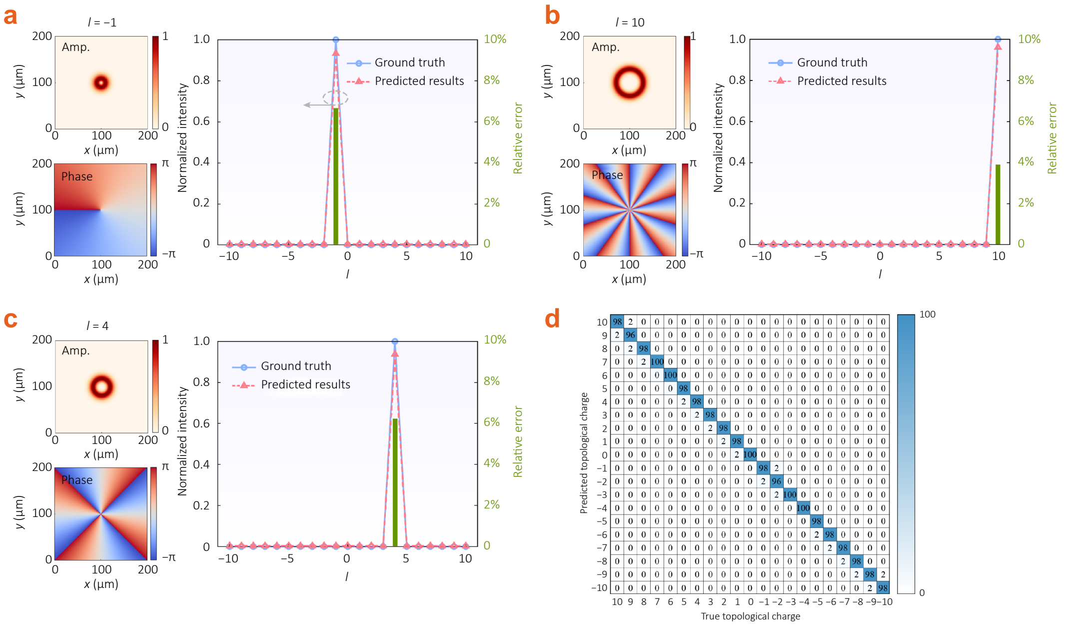

Fig. 3 | Single-mode identification results. Amplitude, phase, and corresponding identification results for (a) $LG_{l = -1, p = 0}$, (b) $LG_{l = 10, p = 0}$, (c) $LG_{l = 4, p = 0}$. (d) Confusion matrix for single-mode identification results.

different spiral phases to regions on the detection plane with phase-sensitive and separable energy distributions, thereby effectively distinguishing ±*l*. This result not only validates the ability of the system to sense and utilize phase information, but also overcomes the inherent limitations of the intensity-based differentiation approach.

3.2 Multi-mode recognition

In a further work, we investigate the recognition performance of the model under multi-mode mixed incident conditions. In particular, we randomly selected mixed beams containing four modes, nine modes, and twenty-one modes to make predictions, as shown in Fig. 4. The phase and amplitude of the four LG beams ($LG_{l = -5, p = 0}$, $LG_{l = -3, p = 0}$, $LG_{l = 5, p = 0}$, $LG_{l = 10, p = 0}$) for superimposed incidence are illustrated in Fig. 4(a). As they are irradiated to the diffraction processor superimposed with equal weights of 0.25, the model output not only accurately determines the various modes of incidence, but also identifies the proportion of each mixed mode based on the distribution of light intensity in each rectangular region, as shown in Fig. 4(b). Similarly, for nine modes of mixed incident light, the model predictions are highly consistent with the true values, as shown in Fig. 4(c-d). The relative error between the model predictions and the true values is less than 3% for LG beams with the equal weighted overlapping incidence, demonstrating excellent multimode decomposition. In addition to equal-proportional mixing, we also validate the performance of the model in handling multiple LG beams mixed with random proportions. Fig. 4(e) shows the amplitude and phase distributions of 21 modes when they are superimposed into the incidence with random weights. Despite the complex distribution of incident light modes, the network is able to accurately recover the intensity weights of each mode with the overall error controlled within 5%, as shown in Fig. 4(f). This result sufficiently proves that the designed network possesses good generalization ability in the face of complex superimposed fields. Rather than only maintaining high robustness with a limited number of mode mixing, it can also adapt to the inhomogeneous mixing of global multi-modes.

Comparing the relative error results of the uniformly weighted mixed beams with those of the randomly weighted mixed beams, we can see that the relative error under the uniformly mixed condition is lower overall and the error distribution is relatively balanced among the modes. This is due to the similar energy contribution of each mode under the uniform mixing condition, which enables the network to obtain a more balanced feature distribution in the output plane. Consequently, the bias phenomenon occurs less frequently during the decoding process, with the overall prediction results stabilized. In contrast, under non-uniform mixing conditions, the energy differences between different modes are significant, resulting in higher overall error rates and larger discrepancies between modes. Further, we count and carefully analyze the mode composition of the non-uniform mixed-mode beams in the training set. We find that for the non-uniformly weighted mixed-mode beams, modes with relatively high errors (e.g., l = −9, 9) are used less frequently in the generated mixed-mode beams, with about 2800 occurrences, whereas modes with lower errors (e.g.,

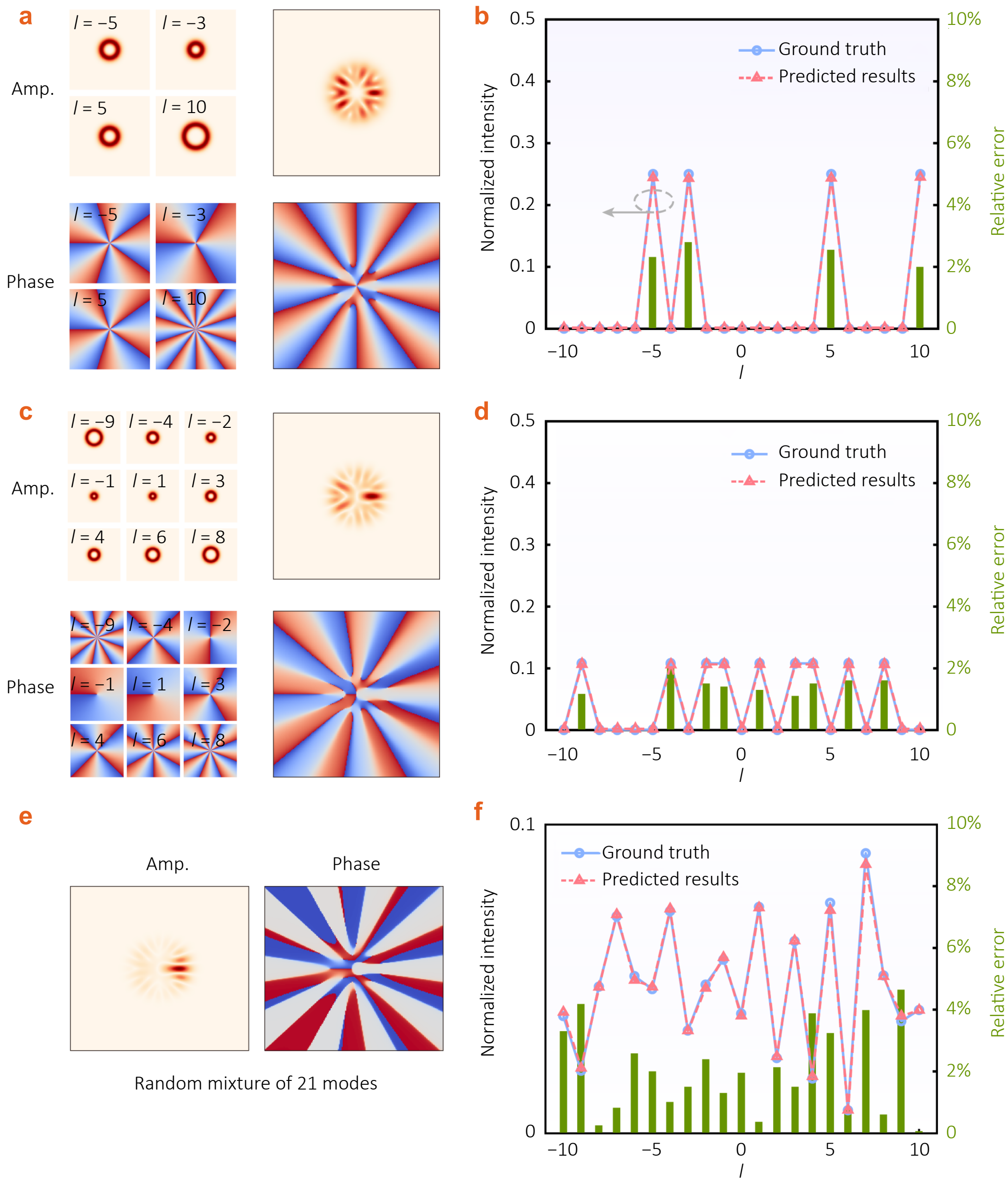

Fig. 4 | Recognition results for multiple modes of mixed incidence. (a) Amplitude and phase of the four LG beams mixed: $LG_{l=-5,\,p=0}$, $LG_{l=-3,\,p=0}$, $LG_{l=5,\,p=0}$, $LG_{l=10,\,p=0}$. (b) Recognition results of four LG beams mixed incidence (c) Amplitude and phase of the nine LG beams: $LG_{l=-9,\,p=0}$, $LG_{l=-4,\,p=0}$, $LG_{l=-2,\,p=0}$, $LG_{l=-1,\,p=0}$, $LG_{l=1,\,p=0}$, $LG_{l=3,\,p=0}$, $LG_{l=4,\,p=0}$, $LG_{l=6,\,p=0}$,$LG_{l=8,\,p=0}$. (d) Recognition results of nine LG beams mixed incidence. (e) Amplitude and phase of randomly mixed incident light for 21 LG beam modes. (f) Recognition results for 21 modes of mixed incidence.

l = −8, 1, 10) are used more frequently, with about 3200 occurrences. This result is consistent with the random selection logic used to generate mixed-mode beams in the dataset, where each mode was randomly selected to participate in the hybrid. The number of times that the different modes of beams appear in the dataset directly affects the ability of the network to learn its features. Modes with a low number of occurrences are underrepresented during training, which reduces the efficiency of the network in learning these modes and leads to increased prediction errors.

3.3 Effects of perturbations on recognition performance

Atmospheric turbulence is one of the key factors contributing to the distortion of OAM beam during propagation, which introduces phase aberrations during beam transmission and leads to corrupted spatial results of OAM. To validate the potential of the proposed system for application in complex environments, we analyze the performance of the model under random atmospheric turbulence perturbations. Specifically, a randomly generated turbulence phase screen is superimposed on the wavefront of the initial incident light to construct turbulent perturbation environments for different scenarios, and these optical fields are input into the model for blind testing. Here we take the modified von Karman model to generate a series of random turbulence phase screens, where the turbulence outer and inner scales are set to 10 m and 0.01 m, respectively, and the refractive index structure constant C_n^2, is varied in the interval from 10^{-15} to 10^{-13}. Figure 5(a) shows the initial amplitude and phase of $\mathrm{LG}_{l=6,\ p=0}$ at the top left, and the generated random turbulent phase screen is shown at the bottom left, along with the phase of the LG beam after being disturbed by turbulence. The model predictions show that the model accurately recognizes the modes despite the turbulence perturbing the vortex phase distribution of the incident light, and its predictions are in agreement with the true values with the relative error remaining at a low level of 2%, as shown in the right-hand side of Fig. 5(a). For uniformly mixed incidence of three and six modes, the relative error remains below 6% and the mode decomposition remains accurate despite the slight increase, as shown in Fig. 5(b-c). When the stacked incident modes are extended to twelve, as shown in Fig. 5(d), in which the complexity of the optical field distribution increases, the irregular phases introduced by the turbulence lead to strong distortions of the original vortex phases. Under this complexity, the correct decomposition of all mode components is achieved, even though the weighting error of individual modes reaches 7%. The outstanding performance of the proposed model in atmospheric turbulence environments shows that the network learns the global orbital angular momentum information hidden in the complex amplitude structure, rather than memorizing local features. This effective learning allows the model to capture complex amplitude features efficiently, which also allows it to extract stable and discriminative information in phase distortion environments, thus realizing reliable recognition of complex optical fields.

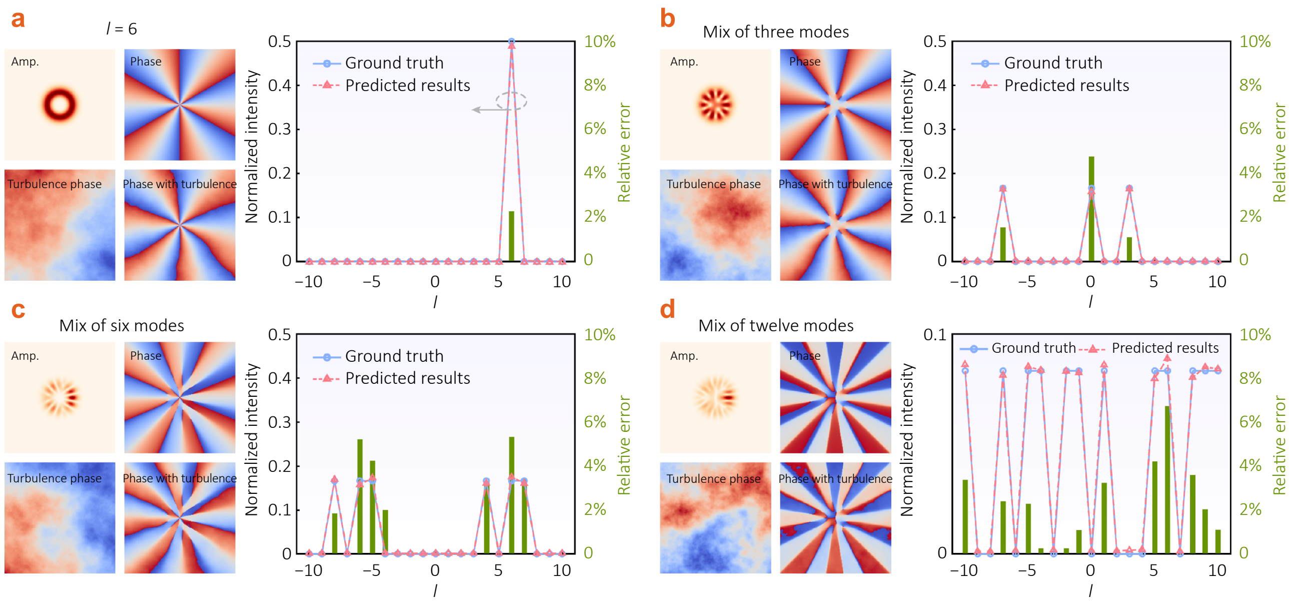

Fig. 5 | Recognition results of the model under atmospheric turbulence perturbation. (a) Identification results for $\mathrm{LG}_{l=6,\ p=0}$ under random turbulent phase perturbations. (b) Recognition results of three-mode mixed beams under random turbulent phase perturbation: $\mathrm{LG}_{l=-7,\ p=0}$, $\mathrm{LG}_{l=0,\ p=0}$, $\mathrm{LG}_{l=3,\ p=0}$. (c) Recognition results of six-mode mixed beams under random turbulent phase perturbation: $\mathrm{LG}_{l=-8,\ p=0}$, $\mathrm{LG}_{l=-6,\ p=0}$, $\mathrm{LG}_{l=-5,\ p=0}$, $\mathrm{LG}_{l=4,\ p=0}$, $\mathrm{LG}_{l=6,\ p=0}$, $\mathrm{LG}_{l=7,\ p=0}$. (d) Recognition results of twelve-mode mixed beams under random turbulent phase perturbation: $\mathrm{LG}_{l=-10,\ p=0}$, $\mathrm{LG}_{l=-7,\ p=0}$, $\mathrm{LG}_{l=-5,\ p=0}$, $\mathrm{LG}_{l=-4,\ p=0}$, $\mathrm{LG}_{l=-2,\ p=0}$, $\mathrm{LG}_{l=-1,\ p=0}$, $\mathrm{LG}_{l=1,\ p=0}$, $\mathrm{LG}_{l=5,\ p=0}$, $\mathrm{LG}_{l=6,\ p=0}$, $\mathrm{LG}_{l=8,\ p=0}$, $\mathrm{LG}_{l=9,\ p=0}$, $\mathrm{LG}_{l=10,\ p=0}$.

4 Conclusions

In summary, we realize a high-precision hybrid OAM modes recognition scheme based on diffractive optical neural network in visible light. As a conceptual demonstration, this work successfully accomplishes the identification of 21 random hybrid spectra of LG beams. Simulation results show that the system maintains high robustness under the perturbation of atmospheric turbulence, demonstrating its potential for applications in the fields of high-capacity optical communication, imaging and sensing under turbulence or complex medium. Minor discrepancies remain between the reconstructed outputs and the target distributions, mainly due to the limited degrees of freedom in the current diffractive structure. These discrepancies may be alleviated by increasing the optical degrees of freedom, such as adding more diffractive layers or enlarging the aperture. They can also be reduced by adopting enhanced training strategies that stabilize the energy distribution across modes. We envision that by increasing the number of diffractive phase screens and the number of phase cells, such OAM beam processor based on diffractive neural network architecture promises to achieve detection and recognition of more states. Implementing the D^{2}NN on programmable metasurfaces enables chip-level compactness and holds promise for achieving amplitude-phase joint modulation, thereby enhancing the recognition capabilities of the system. Meanwhile, the development of an all-optical training strategy is promising to further enhance the system capacity and processing efficiency, opening up new possibilities for the construction of large-scale, scalable OAM information processing platforms.

References

1. Al Ibrahim RH, Zheng SQ, Ng TK et al. Optical image rotation based on orbital angular momentum decomposition and combination. *J Opt* **24**, 115605 (2022).
2. Li MM, Yan SH, Zhang YN et al. Orbital angular momentum in optical manipulations. *J Opt* **24**, 114001 (2022).
3. Andersen MF, Ryu C, Cladé P et al. Quantized rotation of atoms from photons with orbital angular momentum. *Phys Rev Lett* **97**, 170406 (2006).
4. Orlov S, Stanaitis K, Kizevičius P et al. Single-pixel terahertz imaging with enhanced edge detection using angular momentum of structured light. *APL Photonics* **10**, 050805 (2025).
5. Li N, Zheng SL, He T et al. Metasurface-based dual-mode bright-field and spiral phase contrast THz imaging with enhanced focal depth. *J Lightwave Technol* **43**, 4322–4330 (2025).
6. Wang JK, Zhang WH, Qi QQ et al. Gradual edge enhancement in spiral phase contrast imaging with fractional vortex filters. *Sci Rep* **5**, 15826 (2015).
7. Chen SH, Liao Y, Han SJ et al. Joint azimuth-velocity estimation for moving targets with 2-D frequency-mode hopping OAM radar. *IEEE Sens J* **25**, 29053–29063 (2025).
8. Lan H, Xu ZX, Li B et al. Rotational Doppler effect based on reconfigurable circularly polarized OAM array. *IEEE Sens J* **25**, 4503–4510 (2025).
9. Yan HY, Wang JJ, Lei Y et al. Coherent detection of the rotational Doppler effect based on multimode reception. *Opt Laser Technol* **192**, 113425 (2025).
10. Guo YH, Pu MB, Zhao ZY et al. Merging geometric phase and plasmon retardation phase in continuously shaped metasurfaces for arbitrary orbital angular momentum generation. *ACS Photonics* **3**, 2022–2029 (2016).
11. Pu MB, Li X, Ma XL et al. Catenary optics for achromatic generation of perfect optical angular momentum. *Sci Adv* **1**, e1500396 (2015).
12. Chen RS, Wang JH, Zhang XQ et al. Fiber-based mode converter for generating optical vortex beams. *Opto-Electron Adv* **1**, 180003 (2018).
13. Leach J, Padgett MJ, Barnett SM et al. Measuring the orbital angular momentum of a single photon. *Phys Rev Lett* **88**, 257901 (2002).
14. Feng ZK, Wang XY, Dedo MI et al. High-density orbital angular momentum mode analyzer based on the mode converters combining with the modified mach-zehnder interferometer. *Opt Commun* **435**, 441–448 (2019).
15. Zhang Z, Li GY, Liu YL et al. Robust measurement of orbital angular momentum of a partially coherent vortex beam under amplitude and phase perturbations. *Opto-Electron Sci* **3**, 240001 (2024).
16. Ghai DP, Senthilkumaran P, Sirohi RS. Single-slit diffraction of an optical beam with phase singularity. *Opt Lasers Eng* **47**, 123–126 (2009).
17. Dai KJ, Gao CQ, Zhong L et al. Measuring OAM states of light beams with gradually-changing-period gratings. *Opt Lett* **40**, 562–565 (2015).
18. Taira Y, Zhang SK. Split in phase singularities of an optical vortex by off-axis diffraction through a simple circular aperture. *Opt Lett* **42**, 1373–1376 (2017).
19. Huo PC, Yu RX, Liu MZ et al. Tailoring electron vortex beams with customizable intensity patterns by electron diffraction holography. *Opto-Electron Adv* **7**, 230184 (2024).
20. Guo YH, Zhang SC, Pu MB et al. Spin-decoupled metasurface for simultaneous detection of spin and orbital angular momenta via momentum transformation. *Light Sci Appl* **10**, 63 (2021).
21. Dinter T, Li CH, Kühner L et al. Metasurface measuring twisted light in turbulence. *ACS Photonics* **9**, 3043–3051 (2022).
22. Kong LJ, Sun YF, Zhang FR et al. High-dimensional entanglement-enabled holography. *Phys Rev Lett* **130**, 053602 (2023).
23. Zhu SK, Zheng ZH, Meng WJ et al. Harnessing disordered photonics via multi-task learning towards intelligent four-dimensional light field sensors. *PhotoniX* **4**, 26 (2023).
24. Zhao WQ, Wang YN, Ren HY et al. Recent advances in ring-core fiber for orbital-angular-momentum-based mode-division multiplexing. *Opt Commun* **591**, 132091 (2025).
25. Hu JB, Pan HY, Mo XT et al. OAM optical fiber transmission with reduced bit error rate based on turbo code encoding/decoding and deep learning demodulation. *Opt Lasers Eng* **193**, 109061 (2025).
26. Li XY, Chen C, Guo YH et al. Monolithic spiral metalens for ultrahigh-capacity and single-shot sorting of full angular momentum state. *Adv Funct Mater* **34**, 2311286 (2024).
27. Xiong WJ, Luo Y, Liu JM et al. Convolutional neural network assisted optical orbital angular momentum identification of vortex beams. *IEEE Access* **8**, 193801–193812 (2020).
28. Guo YH, Lei YS, Pu MB et al. Vectorial digitelligent optics for high-resolution non-line-of-sight imaging. *Engineering* **45**, 70–78 (2025).
29. Luo XG. Digital optics and optical intelligent agent. *Appl Phys Lett* **127**, 010501 (2025).
30. Zhou R, Guo YH, Zhang Q et al. TurbFPNet: neural far-field turbulent Fourier ptychography with a camera array. *Optica* **12**, 1068–1078 (2025).
31. Ha YL, Luo Y, Pu MB et al. Physics-data-driven intelligent optimization for large-aperture metalenses. *Opto-Electron Adv* **6**, 230133 (2023).
32. Wang JQ, Fu SY, Shang ZJ et al. Adjusted EfficientNet for the diagnostic of orbital angular momentum spectrum. *Opt Lett* **47**, 1419–1422 (2022).
33. Zhu JL, Wu YH, Wang L et al. Measuring the orbital-angular-momentum complex spectrum of light with the fast fourier transform. *Phys Rev Appl* **20**, 014010 (2023).
34. Wang H, Zhan ZY, Hu FT et al. Intelligent optoelectronic processor for orbital angular momentum spectrum measurement. *PhotoniX* **4**, 9 (2023).
35. Lin X, Rivenson Y, Yardimci NT et al. All-optical machine learning using diffractive deep neural networks. *Science* **361**, 1004–1008 (2018).
36. Jiao SM, Liu JW, Zhang LW et al. All-optical logic gate computing for high-speed parallel information processing. *Opto-Electron Sci* **1**, 220010 (2022).
37. Veli M, Mengu D, Yardimci NT et al. Terahertz pulse shaping using diffractive surfaces. *Nat Commun* **12**, 37 (2021).
38. Ye ZY, Zhou CJ, Ding CX et al. Ghost diffractive deep neural networks: optical classifications using light's second-order coherence. *Phys Rev Appl* **20**, 054012 (2023).

39. Li JX, Mengu D, Yardimci NT et al. Spectrally encoded single-pixel machine vision using diffractive networks. *Sci Adv* **7**, eabd7690 (2021).
40. Rahman MSS, Ozcan A. Computer-free, all-optical reconstruction of holograms using diffractive networks. *ACS Photonics* **8**, 3375–3384 (2021).
41. Liao DS, Wang MT, Chan KF et al. A deep-learning enabled discrete dielectric lens antenna for terahertz reconfigurable holographic imaging. *IEEE Antennas Wirel Propag Lett* **21**, 823–827 (2022).
42. Bai BJ, Wei HM, Yang XL et al. Data-class-specific all-optical transformations and encryption. *Adv Mater* **35**, 2212091 (2023).
43. Yang XL, Rahman MSS, Bai BJ et al. Complex-valued universal linear transformations and image encryption using spatially incoherent diffractive networks. *Adv Photonics Nexus* **3**, 016010 (2024).
44. Bai BJ, Luo Y, Gan TY et al. To image, or not to image: class-specific diffractive cameras with all-optical erasure of undesired objects. *eLight* **2**, 14 (2022).
45. Zhao QS, Hao SQ, Wang Y et al. Orbital angular momentum detection based on diffractive deep neural network. *Opt Commun* **443**, 245–249 (2019).
46. Jia Q, Zhang YX, Shi BJ et al. Vector vortex beams sorting of 120 modes in visible spectrum. *Nanophotonics* **12**, 3955–3962 (2023).
47. Allen L, Beijersbergen MW, Spreeuw RJC et al. Orbital angular momentum of light and the transformation of Laguerre-Gaussian laser modes. *Phys Rev A* **45**, 8185–8189 (1992).
48. Yao AM, Padgett MJ. Orbital angular momentum: origins, behavior and applications. *Adv Opt Photonics* **3**, 161–204 (2011).
49. Goodman JW, Cox ME. Introduction to fourier optics. *Phys Today* **22**, 97–101 (1969).

Acknowledgements

This research was supported by National Key Research and Development Program of China (No. 2021YFA1401003), and the National Natural Science Foundation of China (Nos. 62305345, U24A6010, 62222513).

Author contributions

L.-X.G. supervised the whole project. W.-L.J. performed the theoretical calculations and validation. W.-L.J. and W.-J.D. completed the initial structure and network construction. W.-L.J. and W.-J.D. contributed to the results analysis and data processing. W.-L.J. contributed to the data interpretation. W.-J.D. wrote the initial manuscript. W.-L.J., W.-J.D., H.-Y.L., and G.-Y.H. revised and edited the manuscript. All authors contributed to the discussions and preparation of the manuscript.

Competing interests

Xiangang Luo serves as an Editor for the Journal, and no other author has reported any competing interests.